51st AIAA Aerospace Sciences Meeting including the New Horizons Forum and Aerospace Exposition
07 - 10 January 2013, Grapevine (Dallas/Ft. Worth Region), Texas

AIAA 2013-0552

Adjoint-Based Goal-Oriented Mesh Adaptation for Nonequilibrium Hypersonic Flows

Sean R. Copeland*, Amrita K. Lonkar*, Francisco Palacios†, and Juan J. Alonso‡
Dept. of Aeronautics & Astronautics
Stanford University, Stanford, CA, 94305, U.S.A.

Accurately simulating high-speed gas flows requires meshes of high quality. Post shock conditions depend strongly on mesh resolution and must be adequately resolved for accurate force and energy predictions at domain boundaries. Furthermore, the inclusion of multiple chemical constituents and thermochemical nonequilibrium increases the size of the linear system and introduces stiff source terms, placing a premium on efficient solution strategies. This paper proposes such a strategy via adjoint-based goal-oriented mesh adaptation. The adaptation criterion is tuned to a particular functional of interest, enabling optimal grid refinement for continuum, multi-species flow in thermochemical nonequilibrium. The formulation of the direct and continuous adjoint problems is presented, including derivation of the adjoint boundary conditions for pressure-based functionals in multi-species plasmas. Details of the numerical implementation in a general, unstructured CFD solver are also included. Results are presented for an entry velocity, blunt-body geometry in inviscid flow with a two species Nitrogen chemical model. Three adaptation schemes are compared: full grid, gradient-based, and adjoint-based. The goal-oriented adjoint approach exhibits the fastest grid convergence of all methods and higher solution quality when compared to gradient-based adaptation.

Nomenclature

$\vec{A}$	Vector of flux Jacobians
$\vec{d}$	Force projection vector
E	Energy per unit mass
f	Velocity distribution function
$\vec{f}$	Force vector
$\vec{F}$	Flux vector
$\hat{\vec{F}}$	Numerical flux vector
$\vec{f}^{coll}$	Inter-species momentum exchange source term
h	Enthalpy
h_f°	Formation enthalpy
$\bar{\bar{I}}$	Identity matrix
j	Local objective function value
J	Objective function
$\mathcal{J}$	Objective function Lagrangian
k	Boltzmann constant or reaction rate coefficient
K	Equilibrium extent of reaction coefficient
l	Length between nodes

*Ph.D. Candidate, AIAA Student Member.
†Engineering Research Associate, AIAA Member
‡Associate Professor, AIAA Senior Member

n	Number
$\hat{n}$	Unitary normal vector
M	Molar mass
P	Pressure or the conserved to characteristic variable transformation matrix
q	Inter-species energy exchange source term
$q^{inelastic}$	Energy transfer via inelastic collisions
Q	Source term vector
R	Extent of reaction
$\mathcal{R}$	Residual
S	Euler wall boundary of the RAM-C II test case
t	Time
T	Temperature
$\vec{u}$	Velocity
U	Direct solution state vector
$\tilde{U}$	Approximate solution vector
$\dot{w}$	Mass production source term
W	Direct solution characteristic variables
x	Spatial coordinate
Γ	Flow field domain boundaries
ϵ	Energy per unit volume
θ	Characteristic vibrational temperature
λ	Eigenvalues
Λ	Diagonal matrix of eigenvalues
μ	Reduced mass
ν^*	Collision frequency
ξ	Number of degrees of freedom in translational-rotational & vibrational modes
ρ	Density
σ	Collision cross section
τ_{L-T}	Landau-Teller relaxation time
$\vec{\phi}$	Adjoint velocity vector
Ψ	Adjoint solution state vector
Ω	Flow field domain

Subscripts

e	Error
eq	Equilibrium
i	Coordinate direction or node location
j	Coordinate direction or node location
m	Monatomic species
p	Polyatomic species
s	Species
sym	Symmetry
tr	Translational-rotational
vib	Vibrational
∞	Far field

I. Introduction & Motivation

Numerical simulation of high-enthalpy flows in thermochemical nonequilibrium is critical for engineering analysis and design of high-speed flight vehicles. At the current time, the environmental conditions experienced by these vehicles cannot be entirely reproduced in ground testing facilities and the harsh conditions make data acquisition on flight test articles difficult. This places particular importance on the reliability and accuracy of numerical simulations. However, accurately modeling the physical phenomena for these problems requires resolving effects occurring at widely disparate time and length scales, creating a challenging and stiff

numerical problem. Recent comparisons[1] between simulation and experiments continue to show substantial discrepancies, even in regions dominated by laminar, convective heating. The causes of these inaccuracies can be traced to three primary areas:

1. Errors in the aerothermal models
2. Numerical error introduced by the discretization of the governing equations and numerical methods
3. Natural variability (aleatory uncertainty) in entry environments

The issue is compounded by the sparsity of flight relevant datasets for verification and validation of thermochemical models and simulation tools. Consequently, the design process for EDL systems has remained rooted firmly in the procedures established in the 1960s and 70s with proven heritage reliability.

As part of a comprehensive strategy to address this problem, specific goals have been set by NASA's Fundamental Aeronautics Program[2] that include efforts to advance the state-of-the-art in computational aerothermodynamics. These goals include advances in the areas of spatial accuracy, temporal accuracy, unstructured grid technology, mesh adaptation, uncertainty quantification and error control.[3,4] The work presented in this paper supports the goals of the Fundamental Aeronautics Program by addressing the numerical error in aerothermal simulations on unstructured grids via goal-oriented, continuous adjoint-based, adaptive mesh refinement.

Accurate aerothermal solutions require high quality meshes to resolve the conditions behind shock waves and in boundary layers. Current state-of-the-art solvers used by NASA (DPLR, LAURA) utilize structured grids, aligned with the dominant flow features to accurately propagate conserved quantities along streamlines to the vehicle surface. The accuracy of stagnation point heating for 3D simulations on unstructured grids shows a high degree of sensitivity to numerical algorithm settings and mesh quality,[5] especially when compared to structured grid simulations. Adaptive mesh refinement could be an enabling technology for fully unstructured aerothermal solvers, by selectively increasing local mesh density to provide the fidelity necessary to accurately predict heating rates and integrated heat loads to entry systems.

Efforts have been ongoing to explore adaptive mesh refinement techniques for aerothermal simulations and have been met with some success using Discontinuous Galerkin methods, stabilized with artificial viscosity.[6–8] Adjoint-based mesh refinement[9] seems an ideal choice for goal-oriented mesh refinement schemes and has been implemented quite successfully in the low-subsonic to supersonic flight regimes. Comparisons between Hessian-based and adjoint-based mesh refinement schemes[10] have shown that adjoint-based methods can achieve comparable functional accuracy using nearly an order of magnitude fewer grid nodes for supersonic applications.

The progress of adjoint-based methods in the hypersonic regime has been slower, however. The presence of multiple chemical species and stiff source terms for modeling the thermochemical nonequilibrium significantly complicates the implementation of the adjoint solver and makes the derivation of the adjoint equations a daunting task. To alleviate this, discrete adjoint approaches using automatic differentiation tools have been pursued. This approach has been successfully implemented for uncertainty quantification of nonequilibrium entry flow fields[11] and on the full set of coupled magnetohydrodynamic equations.[12] Recent studies[13,14] indicate some potential issues with this methodology. The presence of strong shock waves on misaligned grid topologies have been shown to lead to non-physical oscillatory behavior and can fail to capture the traits of the continuous objective function, regardless of mesh resolution.

In response, this paper pursues a continuous formulation of the adjoint plasma problem, utilizing automatic differentiation tools to acquire the necessary source term Jacobians. This strategy avoids the cited issues associated with discrete adjoint formulations on strongly shocked flows over unstructured grid topologies, and still permits flexibility in the thermochemical modeling, without requiring analytic re-derivation of the source term Jacobians. Section II presents the formulation of the governing equations for the direct problem (with additional modeling details available in Appendices A & B). Section III shows the derivation of the adjoint system with the necessary boundary conditions for acquiring force-based objective function sensitivities. The details of the numerical implementation in a general, unstructured CFD solver are presented in Section IV and the adaptation scheme is discussed in Section V. Adaptation results for an axisymmetric entry body are shown in Section VI with a two species Nitrogen gas chemistry model. Final summary and conclusions can be found in Section VII

II. Direct Problem

This section details the modeling of the entry problem and presents the mathematical formulation of the governing equations. The model proposed departs from the established literature by solving the full set of mass, momentum, energy and vibrational energy conservation equations for each chemical constituent, rather than performing a mass-averaging of the momentum and energy equations in the standard "drift-diffusion" formulation. This approach introduces exchange source terms for momentum and energy and increases the size of the linear system, but is more general and allows for higher degrees of nonequilibrium.

A. Multi-species Euler Model

The direct problem of interest requires modeling a steady, invsicid, compressible, continuum fluid in thermo-chemical nonequilibrium. Each chemical constituent in the multi-species flow field obeys the Euler equations, governing the transport of mass, momentum, and energy throughout the flow domain. For species with internal molecular structure, an additional convection equation for vibrational energy is required. Coupling between the species is handled via source terms that govern the exchange of mass, momentum, energy, and vibrational energy. These source terms are modeled using a combination of experimental conclusions, engineering correlations and by *ab initio* assertions from kinetic theory and statistical mechanics. Explicitly, these equations are,

$$\frac{\partial \rho_s}{\partial t} + \frac{\partial}{\partial x_j}(\rho_s u_{s_j}) = \dot{w}_s, \tag{1a}$$

$$\frac{\partial}{\partial t}(\rho_s u_{s_i}) + \frac{\partial}{\partial x_j}\left(\rho_s u_{s_i} u_{s_j} + P_s \delta_{ij}\right) = f_{s_i}^{coll} + \dot{w}_s u_{s_i}, \tag{1b}$$

$$\frac{\partial \epsilon_s}{\partial t} + \frac{\partial}{\partial x_j}\left((\epsilon_s + P_s) u_{s_j}\right) = f_{s_i}^{coll} u_{s_i} + q_s^{coll} + \dot{w}_s E_s, \tag{1c}$$

$$\frac{\partial \epsilon_{vib_p}}{\partial t} + \frac{\partial}{\partial x_j}\left(\epsilon_{vib_p} u_j\right) = q_p^{inelastic} + \dot{w}_p E_{vib_p}. \tag{1d}$$

Source terms $\dot{w}_s$, $\vec{f}_s^{coll}$, q_s^{coll} and $q_p^{inelastic}$ model the production, destruction, and exchange of mass, momentum, energy, and vibrational energy respectively. Details on the modeling of these terms are included in the appendices.

B. Equations of State

High mach number flow fields contain sufficient energy to excite internal vibrational energy storage modes within polyatomic molecules. Full excitation of these vibrational modes is not typical in low mach number regimes, where the ratio of specific heats, γ, is assumed constant with temperature. To account for these additional energy states, we must include the contributions to total energy from vibrational energy and latent chemical energy ($h_{f_s}^\circ$). We define the energy in the following manner,

$$\epsilon_s = \rho_s E_s = \begin{cases} \rho_s \left(E_{tr_s} + \frac{1}{2} u_{s_i} u_{s_i} + h_{f_s}^\circ\right), & \text{for monatomic species, } s = m. \\ \rho_s \left(E_{tr_s} + E_{vib_s} + \frac{1}{2} u_{s_i} u_{s_i} + h_{f_s}^\circ\right), & \text{for diatomic species, } s = p. \end{cases} \tag{2}$$

Translational-rotational and vibrational energy per unit mass are defined,

$$E_{tr_s} = \frac{\xi_s}{2} \frac{k}{M_s} T_s, \tag{3a}$$

$$E_{vib_s} = \frac{k}{M_s} \frac{\theta_{vib_s}}{e^{\theta_{vib_s}/T_{vib_s}} - 1}, \tag{3b}$$

where corresponding translational-rotational and vibrational temperatures can be determined by inverting Eqns. (3a & 3b). Vibrational energy is modeled as a harmonic oscillator with characteristic vibrational temperature θ_{vib_s}. Partial pressures are assumed to obey the ideal gas law with contribution only from the

translational-rotational states, and mixture pressure obeys Dalton's law of partial pressures

$$P_s = \rho_s \frac{R}{M_s} T_{tr_s}, \tag{4a}$$

$$P = \sum_{s=1}^{n_s} P_s \tag{4b}$$

III. Adjoint Problem

This section describes and formulates the continuous adjoint problem and boundary conditions for the direct equations of Section II. By simulating the full set of Euler equations for each species in the direct problem (with appropriate source term coupling), much of the existing literature on adjoint methods can be leveraged and requires only minor modification to accommodate the re-defined equations of state.

A. Adjoint Equations

The adjoint problem establishes a mathematical framework for determining sensitivities of a specified objective function to large numbers of parameters in an efficient manner. To begin, we choose an objective function of interest. For this work, we focus on integrated projected forces on a surface, S,

$$J = \int_S j(\vec{f}) ds = \int_S \sum_i^{n_s} (\vec{d} \cdot P_i \hat{n}) ds, \tag{5}$$

where $\vec{d}$ is the force projection vector. We require the governing equations of Section II to be satisfied and formulate the analysis in the following way,

$$\begin{aligned} &\textbf{Find} \quad J = \textstyle\int_S j(\vec{f}) ds, \\ &\textbf{such that} \quad \mathcal{R}(U) = 0, \end{aligned} \tag{6}$$

where we have concisely represented Eqns. (1a-1d) in the following form,

$$\mathcal{R}(U) = \nabla \cdot \vec{F}(U) - Q(U) = 0, \qquad \text{in } \Omega, \tag{7a}$$

$$\vec{u} \cdot \hat{n} = 0, \qquad \text{on } S \text{ and } \Gamma_{sym}, \tag{7b}$$

$$W_+ = W_\infty, \qquad \text{on } \Gamma_\infty, \tag{7c}$$

and,

$$U = \left\{ \begin{array}{c} \left(\begin{array}{c} \rho \\ \rho\vec{u} \\ \rho E \\ \rho E_{vib} \end{array} \right)_p \\ \vdots \\ \left(\begin{array}{c} \rho \\ \rho\vec{u} \\ \rho E \end{array} \right)_m \\ \vdots \end{array} \right\}, \quad \vec{F}(U) = \left\{ \begin{array}{c} \left(\begin{array}{c} \rho\vec{u} \\ \rho\vec{u} \otimes \vec{u} + P\bar{\bar{I}} \\ \rho\vec{u}h \\ \rho\vec{u}E_{vib} \end{array} \right)_p \\ \vdots \\ \left(\begin{array}{c} \rho\vec{u} \\ \rho\vec{u} \otimes \vec{u} + P\bar{\bar{I}} \\ \rho\vec{u}h \end{array} \right)_m \\ \vdots \end{array} \right\}, \quad Q(U) = \left\{ \begin{array}{c} \left(\begin{array}{c} \dot{w} \\ \vec{f}^{coll} + \dot{w}\vec{u} \\ (\vec{f}^{coll} \cdot \vec{u}) + q^{coll} + \dot{w}E \\ q^{inelastic} + \dot{w}E_{vib} \end{array} \right)_p \\ \vdots \\ \left(\begin{array}{c} \dot{w} \\ \vec{f}^{coll} + \dot{w}\vec{u} \\ (\vec{f}^{coll} \cdot \vec{u}) + q^{coll} + \dot{w}E \end{array} \right)_m \\ \vdots \end{array} \right\},$$

$$\begin{aligned} \text{for } p \quad &= 1, 2, ..., n_p, \\ \text{and for } m \quad &= 1, 2, ..., n_m. \end{aligned}$$

By satisfying the governing equations, $\mathcal{R}(U) = 0$, this equality-constrained analysis can be transformed to an unconstrained problem via the addition of an inner product of the adjoint variables with the governing equations to form the Lagrangian,

$$\mathcal{J} = \int_S j(\vec{f}) ds - \int_\Omega \Psi^T \mathcal{R}(U) d\Omega, \tag{8}$$

where we have introduced the adjoint variables Ψ as Lagrange multipliers to the linear system,

$$\Psi = \left\{ \begin{array}{c} \left(\begin{array}{c} \psi_\rho \\ \psi_{\rho u} \\ \psi_{\rho v} \\ \psi_{\rho E} \\ \psi_{\rho E_{vib}} \end{array} \right)_p \\ \vdots \\ \left(\begin{array}{c} \psi_\rho \\ \psi_{\rho u} \\ \psi_{\rho v} \\ \psi_{\rho E} \end{array} \right)_m \end{array} \right\} = \left\{ \begin{array}{c} \left(\begin{array}{c} \psi_\rho \\ \vec{\phi} \\ \psi_{\rho E} \\ \psi_{\rho E_{vib}} \end{array} \right)_p \\ \vdots \\ \left(\begin{array}{c} \psi_\rho \\ \vec{\phi} \\ \psi_{\rho E} \end{array} \right)_m \end{array} \right\}, \qquad \begin{array}{l} \text{for } p = 1, 2, ..., n_p, \\ \text{for } m = 1, 2, ..., n_m. \end{array} \tag{9}$$

To determine the effect that changes in the flow field have on our objective function, we take the first variation of the Lagrangian,

$$\delta \mathcal{J} = \int_S \delta j(\vec{f}) ds - \int_\Omega \Psi^T \delta \mathcal{R}(U) d\Omega. \tag{10}$$

Explicitly, the final term in Eq. (10) can be expressed as,

$$\int_\Omega \Psi^T \delta \mathcal{R}(U) d\Omega = \int_\Omega \Psi^T (\nabla \cdot \vec{A}) \delta U d\Omega - \int_\Omega \Psi^T \frac{\partial Q}{\partial U} \delta U d\Omega \tag{11}$$

where $\vec{A} = \frac{\partial \vec{F}}{\partial U} = (\frac{\partial F_x}{\partial U}, \frac{\partial F_y}{\partial U}, \frac{\partial F_z}{\partial U})$.

By applying integration by parts and the divergence rule, the domain integral can be split into domain and boundary components.

$$\begin{aligned} \int_\Omega \Psi^T (\nabla \cdot \vec{A}) \delta U d\Omega &= \int_\Omega \nabla \cdot (\Psi^T \vec{A} \delta U) d\Omega - \int_\Omega \nabla \Psi^T \cdot \vec{A} \delta U d\Omega \\ &= \int_\Gamma (\Psi^T \vec{A} \delta U) \cdot \hat{n} ds - \int_\Omega \nabla \Psi^T \cdot \vec{A} \delta U d\Omega. \end{aligned} \tag{12}$$

Inserting Eqn. (12) in to Eqn. (10),

$$\delta \mathcal{J} = \int_S \delta j(\vec{f}) ds - \int_\Gamma (\Psi^T \vec{A} \delta U) \cdot \hat{n} ds + \int_\Omega \left[\nabla \Psi^T \cdot \vec{A} + \Psi^T \frac{\partial Q}{\partial U} \right] \delta U d\Omega. \tag{13}$$

By setting the integrand of the domain integral to zero, we eliminate the functional dependence of the variation of the objective function to variations in the domain flow solution, δU. For convenience, we take the transpose to arrive at the adjoint system of equations,

$$\vec{A}^T \cdot \nabla \Psi + \frac{\partial Q}{\partial U}^T \Psi = 0. \tag{14}$$

B. Adjoint Boundary Conditions

The integral over domain boundaries, Γ, in Eqn. (13), must be specified to form a well-posed problem. If chosen carefully, these adjoint boundary conditions can be used to eliminate the functional dependence of the variation in the objective function, $\mathcal{J}$, to variations in the state variables, δU.

Let us consider the domain integral on, S,

$$\begin{aligned} \int_S (\Psi^T \vec{A} \delta U) \cdot \hat{n} ds &= \int_S (\Psi^T (\vec{A} \cdot \hat{n}) \delta U ds \\ &= \int_S \sum_i^{n_s} (\vec{\phi}_i \cdot \hat{n}) \delta P_i ds + \int_S \sum_i^{n_s} (\delta \vec{u}_i \cdot \hat{n}) \rho_i \nu_i, \end{aligned} \tag{15}$$

where we have performed the matrix vector product using the definition of the projected flux Jacobian, $\vec{A}\cdot\hat{n}$, and enforced the flow tangency boundary conditions $\vec{u}_i \cdot \hat{n} = 0$. The quantity ν is defined,

$$\nu_i = \psi_{\rho_i} + (\vec{\phi}_i \cdot \vec{u}_i) + \psi_{\epsilon_i}\frac{\epsilon_i + P_i}{\rho_i} + \psi_{\epsilon_{vib_i}}\frac{\epsilon_{vib_i}}{\rho_i} \qquad \text{for } i = 1, ..., n_s.$$

By linearizing the boundary conditions ($\vec{u}' = \vec{u} + \delta\vec{u}$), we eliminate the second term in Eqn. (15),

$$\vec{u}' \cdot \hat{n} = (\vec{u} + \delta\vec{u}) \cdot \hat{n} = 0 \tag{16}$$
$$= \vec{u} \cdot \hat{n} + \delta\vec{u} \cdot \hat{n} = 0 \tag{17}$$
$$= \delta\vec{u} \cdot \hat{n} = 0 \tag{18}$$

and we are left with,

$$\int_S \left[(\vec{d} \cdot \hat{n}) - (\vec{\phi} \cdot \hat{n})\right] \delta P ds. \tag{19}$$

We eliminate the dependence of $\delta\mathcal{J}$ to δP on S by choosing,

$$\vec{d} \cdot \hat{n} = \vec{\phi} \cdot \hat{n} \qquad \text{on } S \tag{20}$$

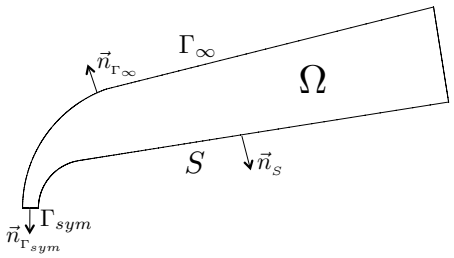

Figure 1. Schematic of the computational domain, boundary conditions and surface normals for a representative axisymmetric body of revolution.

By following the same procedure we arrive at an identical adjoint boundary condition on Γ_{sym}. For the far field boundary conditions, we enforce $\Psi = 0$. In summary, the adjoint problem on the domain of Fig. (1) is as follows:

$$\vec{A}^T \cdot \nabla\Psi + \frac{\partial Q}{\partial U}^T \Psi = 0 \qquad \text{in } \Omega, \tag{21a}$$
$$\vec{d} \cdot \hat{n} = \vec{\phi} \cdot \hat{n} \qquad \text{on } S, \tag{21b}$$
$$\vec{\phi} \cdot \hat{n} = 0 \qquad \text{on } \Gamma_{sym}, \tag{21c}$$
$$\Psi = 0 \qquad \text{on } \Gamma_\infty. \tag{21d}$$

IV. Simulation Methodology

The direct and adjoint problems formulated in Sections II & III governing continuum, compressible, inviscid, multi-component flows in thermochemical nonequilibrium were implemented in the Stanford University Unstructured[15] (SU^2) software suite. This open-source, C++ based software package is particularly well suited to performing PDE-analysis and PDE-constrained optimization on unstructured grid topologies. The architecture of the code supports complex multi-physics simulations and is particularly well suited to the problem at hand.

Both the direct and adjoint problems require the Jacobian of the source terms $\frac{\partial Q}{\partial U}$. These source terms depend on the choice of thermochemical models, the selected gas model, and can often be quite complex. To permit flexibility and rapid implementation of new models, these Jacobians are determined using Automatic Differentiation (AD) tools. Since the source terms are evaluated on a cell-by-cell basis, this AD approach is still consistent with the continuous adjoint formulation in the previous section.

A. Discretization of the Governing Equations

The direct and adjoint solutions are solved using a node-centered, edge-based, Finite Volume Method (FVM). The spatial discretization utilizes one of several first order schemes, including Roe,[16] Steger-Warming,[17] and Lax-Friedrich[18] with implicit Euler time marching. This discretization is obtained by applying the integral formulation of the augmented Euler equations to a dual grid control volume Ω_i surrounding node i and performing exact integration on the boundaries. Using the divergence theorem and a fully discrete approximation of the temporal derivative we arrive at

$$|\Omega_i|\frac{U_i^{n+1} - U_i^n}{\Delta t} + \sum_{j=1}^{m_i} \hat{\vec{F}}_{ij} \cdot \vec{n}_{ij} l_{ij} - |\Omega_i| Q_i = 0, \tag{22}$$

where $\hat{\vec{F}}$ are the convective numerical fluxes, Q is the vector of source terms, $|\Omega_i|$ is the cell area (or volume in 3D) of Ω_i, $\vec{n}_{ij}$ is the outward unit vector normal to the face associated with the grid edge connecting i and j, l_{ij} is the length of the edge between i and j (or area in 3D), and m_i is the number of neighbors of the node i.

Convective fluxes, from node i to node j across dual grid interfaces, are reduced to one dimensional problems by projecting onto the unit normal between the nodes,

$$\hat{\vec{F}}_{ij}^{Roe} = \frac{1}{2}\left(\vec{F}_i + \vec{F}_j\right)\cdot\vec{n}_{ij} - \frac{1}{2}|\bar{\bar{A}}_{ij}|(U_j - U_i), \tag{23a}$$

$$\hat{\vec{F}}_{ij}^{SW} = \bar{\bar{A}}_i^{+}U_i + \bar{\bar{A}}_j^{-}U_j, \tag{23b}$$

$$\hat{\vec{F}}_{ij}^{LF} = \frac{1}{2}\left(\vec{F}_i + \vec{F}_j\right)\cdot\vec{n}_{ij} + \epsilon_0\lambda(U_i - U_j), \tag{23c}$$

$$\tag{23d}$$

where $\lambda = \frac{1}{2}[(\vec{v_i}\cdot n_{ij} + c_i) + (\vec{v_j}\cdot n_{ij} + c_j)]$, and ϵ_0 is an artificial dissipation parameter. The adjoint equations, Eqn. (14), are discretized in space and time similarly.

For the upwind schemes, the flux Jacobian, $\bar{\bar{A}}$, is calculated using an eigenvalue decomposition,

$$\bar{\bar{A}} = P^{-1}|\Lambda|P, \tag{24a}$$

$$\bar{\bar{A}}^{\pm} = P^{-1}|\Lambda^{\pm}|P. \tag{24b}$$

where P, P^{-1}, and Λ are block diagonal to accommodate each of the gas species,[19]

$$P = \begin{vmatrix} P_{N_2} & 0 & \dots & 0 \\ 0 & P_{O_2} & 0 & \vdots \\ \vdots & 0 & \ddots & 0 \\ 0 & \dots & 0 & P_{e^-} \end{vmatrix}, \quad P^{-1} = \begin{vmatrix} P_{N_2}^{-1} & 0 & \dots & 0 \\ 0 & P_{O_2}^{-1} & 0 & \vdots \\ \vdots & 0 & \ddots & 0 \\ 0 & \dots & 0 & P_{e^-}^{-1} \end{vmatrix}, \quad \Lambda = \begin{vmatrix} \Lambda_{N_2} & 0 & \dots & 0 \\ 0 & \Lambda_{O_2} & 0 & \vdots \\ \vdots & 0 & \ddots & 0 \\ 0 & \dots & 0 & \Lambda_{e^-} \end{vmatrix}.$$

A calculation of the source term Jacobian, $\frac{\partial Q}{\partial U}$, is required in both the implicit direct and adjoint solvers. Analytical expressions for the terms in the Jacobian are the most computationally efficient, but can be quite complex, and in some cases, impossible due to the widespread use of tabulated thermochemical data. Additionally, great precision in the Jacobians is necessary for the stability of the direct and adjoint solvers, as some chemical constituents can be present in trace amounts depending on the runtime free stream conditions. For this work, an AD approach using TAPENADE[20] is taken, applied to the numerical implementation of the source terms within SU^2. This method gives great flexibility for the selection and implementation of different thermochemical models and is not subject to the weaknesses of the finite-difference method.

V. Grid Adaptation Methodology

The error estimate of integral outputs of partial differential equations can be used as indicators for goal-oriented grid adaptation. These techniques produce good (and even optimal) numerical grids for the accurate estimation of an output functional. Consider a nonlinear functional, $\mathcal{J}(U)$, (e.g. integrated heat flux or integrated projected forces on a body surface), where U is the exact solution of a set of nonlinear equations[21]

$$\mathcal{R}(U) = 0.$$

Given an approximate solution, $\tilde{U}$, we define U_ϵ as the error of the solution, $U_\epsilon = \tilde{U} - U$, and linearize both the nonlinear equation and the functional:

$$\mathcal{R}(\tilde{U}) = \mathcal{R}(U + U_\epsilon) \approx \mathcal{R}(U) + \frac{\partial \mathcal{R}}{\partial U}U_\epsilon = \frac{\partial \mathcal{R}}{\partial U}U_\epsilon, \tag{25a}$$

$$\mathcal{J}(\tilde{U}) = \mathcal{J}(U + U_\epsilon) \approx \mathcal{J}(U) + \frac{\partial \mathcal{J}}{\partial U}U_\epsilon. \tag{25b}$$

From Eqn. (8),

$$\frac{\partial \mathcal{J}}{\partial U} = \Psi^T \frac{\partial \mathcal{R}}{\partial U}, \tag{26}$$

and inserting into Eqn. (25b),

$$\mathcal{J}(\tilde{U}) = \mathcal{J}(U) + \Psi^T \frac{\partial \mathcal{R}}{\partial U} U_\epsilon = \mathcal{J}(U) + \Psi^T \mathcal{R}(\tilde{U}), \tag{27}$$

where $\mathcal{J}(\tilde{U}) - \Psi^T \mathcal{R}(\tilde{U})$ is a more accurate estimate for $\mathcal{J}(U)$ than $\mathcal{J}(\tilde{U})$. We will use this *computable correction* $\Psi^T \mathcal{R}(\tilde{U})$ as a sensor for our goal oriented adaptation. The entire methodology is described below.

1. Solve the multi-species Euler equations on the numerical grid.
2. Solve the adjoint problem for Ψ.
3. Perform a full, homothetic subdivision of the numerical grid and compute the residual of the direct problem.
4. Compute the adaptation estimator for each node by taking an inner product of the adjoint variables and the direct problem residuals on the fine grid.
5. Refine the grid according the specifications.
6. Repeat.

The grid adaptation software permits subdivision of both triangular and rectangular cells for two-dimensional and axisymmetric simulations. The refinement schemes for both cell types is shown in Fig. (2). Hanging nodes are not allowed and the solver supports only quad and triangle-based meshes in two dimensions. As a consequence, a buffer region is created in cells adjacent to the adapted cells. This buffer region is particularly apparent during refinement of the quad-based grid, as triangles become introduced into the computational flow domain.

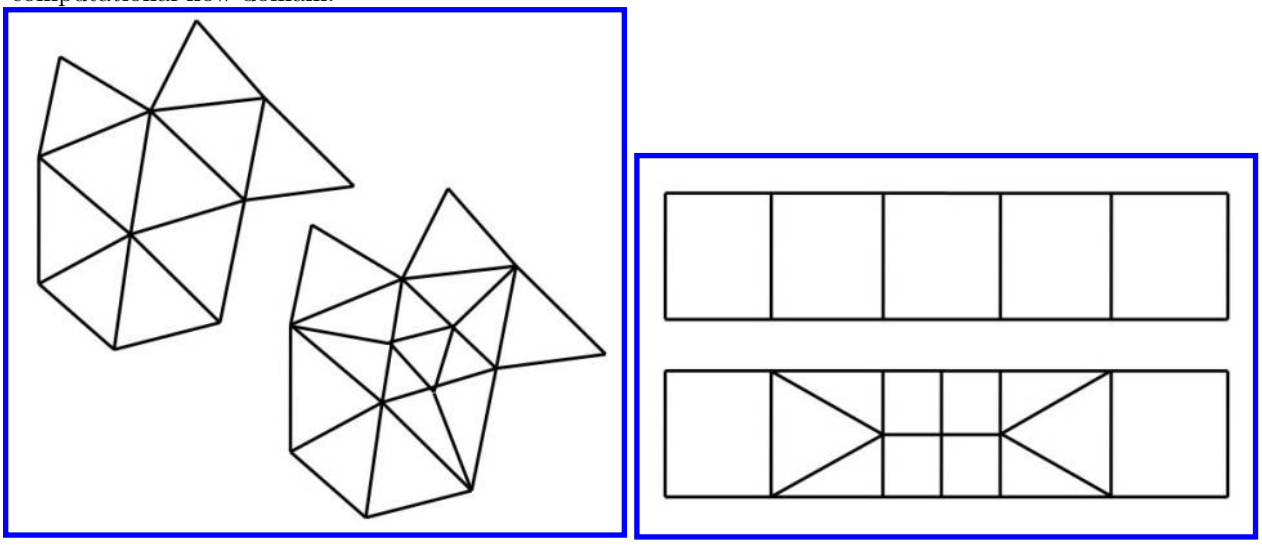

(a) Triangle adaptation. (b) Quad adaptation.

Figure 2. Adaptation schemes for triangles and quads and their buffer regions.

VI. Results

To test the utility of the goal-oriented, adjoint-based approach to mesh adaptation for multi-species plasmas, a grid convergence study was performed using three adaptation schemes: full grid, gradient-based, and adjoint-based. The problem selected is based on a series of hypersonic flight tests[22] conducted at NASA

to quantify electron number densities around entry vehicles. The RAM-C II test article in that test series is of particular interest due to the non-ablative, beryllium nose, making it an ideal candidate for verification and validation of computational tools. The test vehicle was equipped with four microwave reflectometers and an electrostatic rake that measured electron number densities at four axial locations along the vehicle and through the boundary layer. RAM-C II geometry and experimental conditions are provided in Tab. (1) & (2).

Table 1. RAM-C II Geometry

Nose Radius	$0.1524m$
Cone Half Angle	9°
Vehicle Length	$1.295m$

Table 2. RAM-C II Flight Conditions

	Case 5	Case 6	Case 7
H (km)	61	71	81
T_∞ (K)	254	216	181
R_e	19500	6280	1590
$\mathcal{M}_\infty$	23.9	25.9	28.3

All simulation results presented are performed using an invsicid, two-species Nitrogen gas chemistry model at the free stream conditions of Case 6 in Tab. (2). Direct problem solutions utilize the first-order Steger-Warming spatial discretization scheme with implicit Euler time marching. Adjoint solutions for the goal-oriented adaptation strategy use the drag coefficient as the objective function and first-order Roe spatial discretization. All solutions are converged 6 orders of magnitude in the N_2 density residual, with the convergence history from each of the finest grid solutions shown in Fig. (3).

Results from the three adaptation strategies are displayed here: full flow, flow gradient-based, and "computable error" adjoint-based. A comparison of the different strategies and the value of the drag coefficient is plotted against mesh sizes for each of the adaptation strategies in Fig. (4). Each mark in the plot denotes another cycle of adaptation, with a total of four cycles performed using the full grid approach, eight using the gradient based method and five using the adjoint method. Full grid adaptations perform homothetic subdivisions of every cell in the computational domain, increasing the total cell count by a factor of four at each cycle. The gradient and adjoint methods add 50% more cells at each revision of the mesh. Both the gradient and adjoint approaches show rapid convergence of the grid (within 5-6 adaptation cycles), with far fewer nodes than using the full-grid approach, which is still not converged, even when the number of cells has increased by more than 250 times the baseline value. This immediately demonstrates the utility of both gradient and adjoint-based methodologies to perform shock capturing in hypersonic, multi-species flows.

Table 3. Converged mesh sizes

Adaptation Strategy	Adaptation Cycles	Node Count
Baseline	N/A	1105
Full Grid	4+	263425
Gradient-based	6	18195
Adjoint-based	5	11773

A comparison of the resulting adapted meshes using the three strategies is shown in Fig. (5). Note the differences between the gradient and adjoint-based refinements. The highest flow gradients are behind the strong, detached shock and the gradient method refines these cells highly, but ignores the rest of the domain, whereas the adjoint approach performs refinement along the shock, as well as on the body surface to resolve

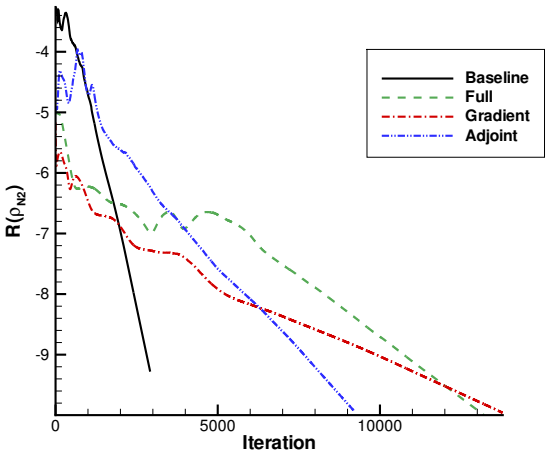

Figure 3. Log-reduction in density residual for the most highly adapted meshes.

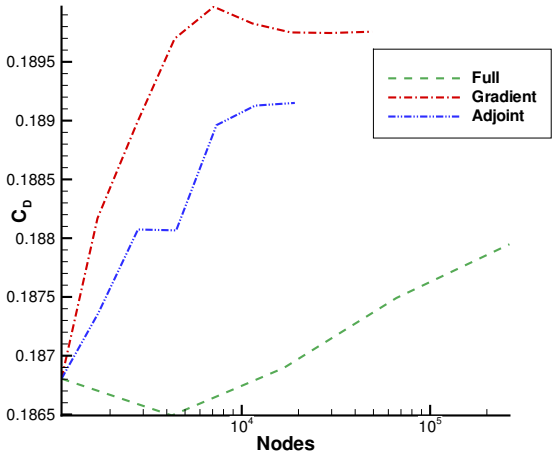

Figure 4. C_D convergence for the adaptation schemes.

flow gradients necessary for accurate projected force computations on the surface.

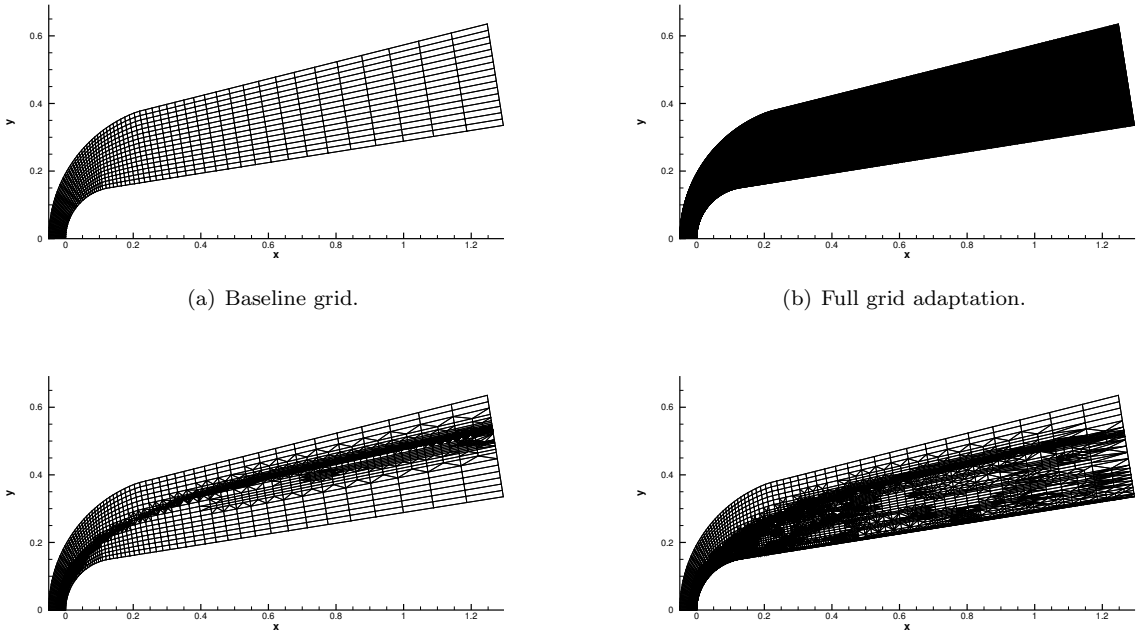

(a) Baseline grid.

(b) Full grid adaptation.

(c) Gradient-based adaptation.

(d) Adjoint-based adaptation.

Figure 5. Adapted meshes.

As seen in Fig. (6), the gradient and adjoint schemes introduce triangular cells as buffer regions are generated during each adaptation cycle. For the gradient strategy, these buffer region cells become highly anisotropic as the grid further refines the shock region and solution quality suffers. The adjoint approach, on the other hand, exhibits some of these traits, but solution quality is much higher (based on measures of shock standoff distance and post-shock temperatures, that can be seen in Fig. (7)).

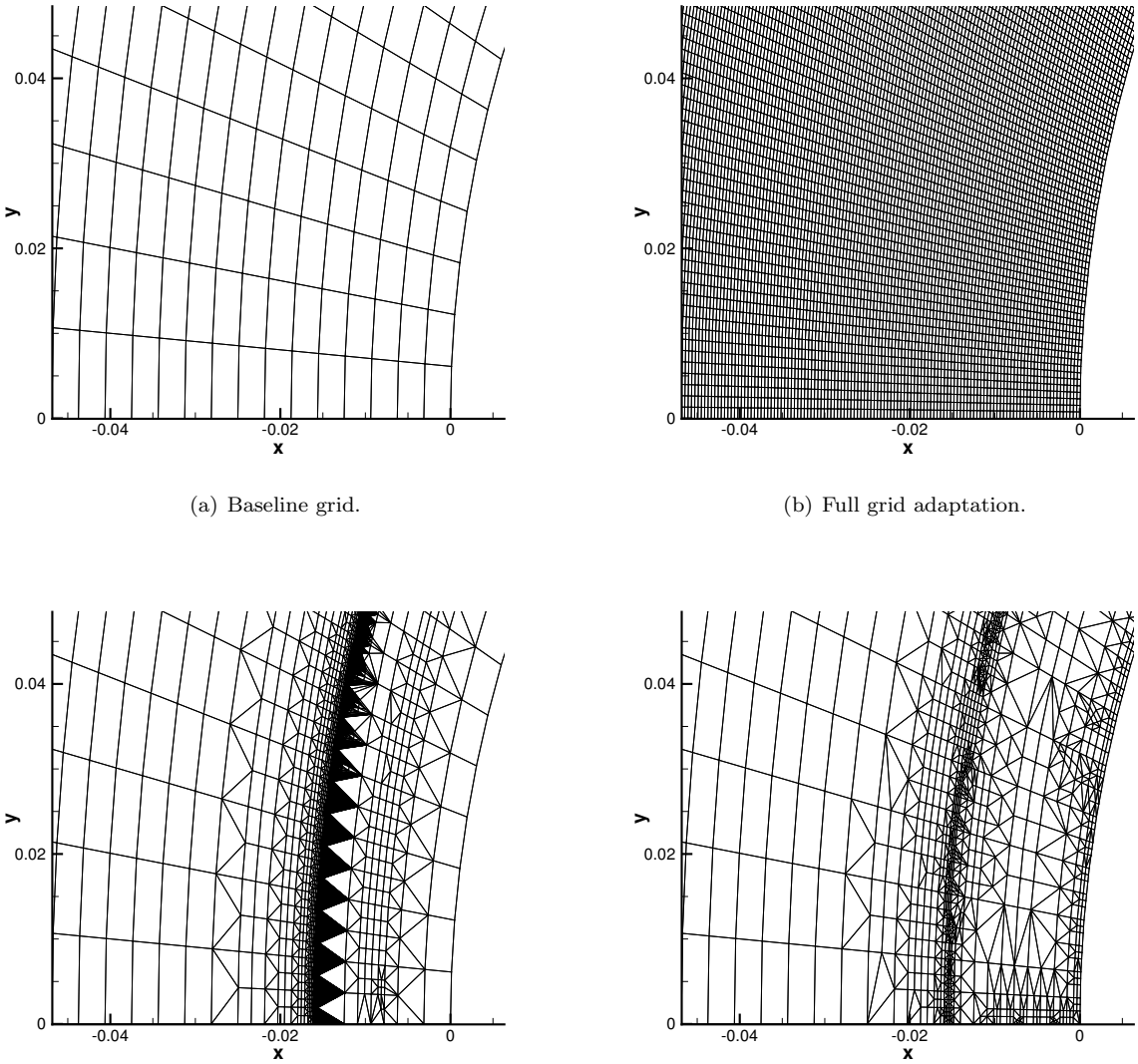

(a) Baseline grid.

(b) Full grid adaptation.

(c) Gradient-based adaptation.

(d) Adjoint-based adaptation.

Figure 6. Zoomed view of the adapted grids, showing differences in mesh topologies and adaptation strategies.

VII. Conclusion

The development of adaptive mesh refinement methodologies for hypersonic applications have the potential to be enabling technologies for high-quality, unstructured aerothermal simulations. Goal-oriented, adjoint-based approaches have exhibited superior performance when compared to other adaptive schemes to predict functional values for subsonic and supersonic regimes, however the adjoint formulation for the augmented Euler equations with thermochemical nonequilibrium source terms are more complex and numerically stiff. Furthermore, discrete adjoint methods have shown inaccuracies in predicting sensitivities in the presence of strong shock waves on grids with cell boundaries misaligned with large-scale flow features. In this work, the formulation and derivation of the continuous adjoint problem with the necessary boundary conditions is presented for continuum, inviscid, multi-species flows in thermochemical nonequilibrium.

Results demonstrated the capability of the solver to perform direct and adjoint solutions at high Mach numbers using common upwinding and centered spatial discretization schemes and directly compare the adjoint, gradient and full mesh adaptation methods. While the full scheme showed the highest solution

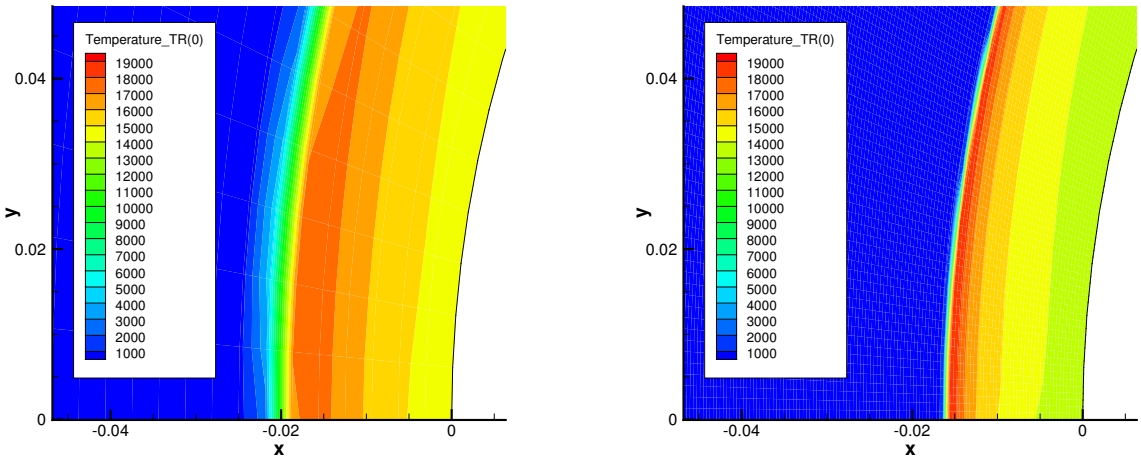

(a) Baseline grid.

(b) Full grid adaptation.

(c) Gradient-based adaptation.

(d) Adjoint-based adaptation.

Figure 7. Adaptation behind the shock at the nose of the RAM-C II geometry.

quality by preserving the quadrilateral grid topology, reaching grid convergence required too many cells, even for the simple test case and two species gas model, making this option infeasible for more complex problems. The gradient based approach showed rapid convergence in the objective function, but the introduction of the buffer region, dominated by adaptation behind the strong shock wave resulted in poor solution quality in the post-shock region. The adjoint approach also showed rapid convergence, while maintaining higher solution quality when compared to the gradient approach, and is the clear winner among the three adaptation schemes. The presence of the buffer region in the flow domain degraded solution quality for both the gradient and adjoint refinement schemes, as was expected given the grid misalignment with the strong flow gradients. Different buffer region adaptation strategies must be pursued or eliminated by allowing arbitrary polyhedra in unstructured aerothermal solvers to preserve solution quality on the adapted meshes.

Acknowledgments

Sean R. Copeland would like to thank Mr. and Mrs. John Lillie for their generous contributions to the Stanford Graduate Fellowship program, through which this research was funded. He would also like to thank Todd White and Deepak Bose of NASA's Ames Research Center for their guidance and suggestions pertaining to high-fidelity aerothermal CFD. Amrita K. Lonkar would like to acknowledge her support from the Stanford Graduate Fellowship program.

References

[1]Hollis, B. and Prabhu, D., "Assessment of Laminar, Convective Aeroheating Prediction Uncertainties for Mars Entry Vehicles," *42nd AIAA Thermophysics Conference*, AIAA Paper 2011-3144, Honolulu, HI, 2011.

[2]Mansour, N., Pittman, J., and Olson, L., "Fundamental Aeronautics Hypersonics Project: Overview," *39th AIAA Thermophysics Conference*, AIAA Paper 2007-4263, Miami, FL, June 2007.

[3]Bose, D., "Hypersonic Aerodynamics, Aerothermodynamics and Plasmadynamics Research Activities within NASA's Fundamental Aeronautics Program," *16th AIAA/DLR/DGLR International Space Planes and Hypersonic Systems and Technologies Conference*, AIAA Paper 2009-7278, Bremen, Germany, 2009.

[4]Salas, M., "A Review of Hypersonics Aerodynamics, Aerothermodynamics and Plasmadynamics Activities within NASA's Fundamental Aeronautics Program," *39th AIAA Thermophysics Conference*, AIAA Paper 2007-4264, Miami, FL, June 2007.

[5]Gnoffo, P. and White, J., "Computational Aerothermodynamic Simulation Issues on Unstructured Grids," *37th AIAA Thermophysics Conference*, AIAA Paper 2004-2371, Portland, OR, 2004.

[6]Barter, G. E. and Darmofal, D. L., "Shock Capturing with Higher-Order, PDE-Based Artificial Viscosity," *18th AIAA Computational Fluid Dynamics Conference*, AIAA Paper 2007-3823, Miami, FL, 2007.

[7]Barter, G. E., *Shock Capturing with PDE-Based Artificial Viscosity for an Adaptive Higher-Order Discontinuous Galerkin Finite Element Method*, Ph.D. thesis, Massachusetts Inst. of Technology, 2008.

[8]Fidkowski, K. J. and Darmofal, D. L., "Review of Output-Based Error Estimation and Mesh Adaptation in Computational Fluid Dynamics," *AIAA Journal*, Vol. 49, No. 4, 2011, pp. 673–694.

[9]Park, M. A., "Adjoint-Based, Three-Dimensional Error Prediction and Grid Adaptation," *32nd AIAA Fluid Dynamics Conference*, AIAA Paper 2002-3286, St. Louis, MO, June 2002.

[10]Gnoffo, P., "Computational Fluid Dynamics Technology for Hypersonic Applications," *AIAA/ICAS International Air and Space Symposium and Exposition: The Next 100 Years*, AIAA Paper 2003-2829, Dayton, OH, 2003.

[11]Lockwood, B., Rumpfkeil, M., Yamazaki, W., and Mavriplis, D., "Uncertainty Quantification in Viscous Hypersonic Flows using Gradient Information and Surrogate Modeling," *49th AIAA Aerospace Science Meeting including the New Horizons Forum and Aerospace Exposition*, AIAA Paper 2011-885, Orlando, FL, Jan. 2011.

[12]Marta, A., *Rapid Development of Discrete Adjoint Solvers with Applications to Magnetohydrodynamic Flow Control*, Ph.D. thesis, Stanford University, 2007.

[13]Bueno-Orovio, A., Castro, C., Duraisamy, K., Palacios, F., and Zuazua, E., "When the 'exact' discrete gradient is not the best choice in optimal shape design?" *49th AIAA Aerospace Science Meeting including the New Horizons Forum and Aerospace Exposition*, AIAA Paper 2011-1298, Orlando, FL, 2011.

[14]Giles, M., Duta, M., Müller, J., and Pierce, N., "Algorithm Developmetns for Discrete Adjoint Methods," *AIAA Journal*, Vol. 41, No. 2, 2003, pp. 198–205.

[15]Palacios, F., Colonno, M. R., Aranake, A. C., Campos, A., Copeland, S. R., Economon, T. D., Lonkar, A. K., Lukaczyk, T. W., Taylor, T. W. R., and Alonso, J. J., "Stanford University Unstructured (SU^2): An open-source integrated computational environment for multi-physics simulation and design." *51st Aerospace Sciences Meeting Including the New Horizons Forum and Aerospace Exposition*, AIAA Paper 2013-0287, Grapevine, TX, 2013.

[16]Roe, P. L., "Approximate Riemann Solvers, Parameter Vectors and Difference Schemes," *Journal of Computational Physics*, Vol. 43, 1981, pp. 357–372.

[17]Steger, J. L. and Warming, R. F., "Flux Vector Splitting of the Inviscid Gasdynamic Equations with Application to Finite-Difference Methods," *Journal of Computational Physics*, Vol. 40, 1981, pp. 263–293.

[18]Lax, P. D., "Weak Solutions of Nonlinear Hyperbolic Equations and Their Numerical Computation," *Communications on Pure and Applied Mathematics*, Vol. 7, 1954, pp. 159–193.

[19]Hirsch, C., *Numerical Computation of Internal and External Flows. Volume 2: Computation Methods for Inviscid and Viscous Flows*, Wiley, 1990.

[20]Hascoët, L., "TAPENADE: a tool for Automatic Differentiation of programs," *Proceedings of 4^{th} European Congress on Computational Methods, ECCOMAS'2004, Jyvaskyla, Finland*, 2004.

[21]Giles, M. B. and Pierce, N. A., "Adjoint error correction for integral outputs," Error Estimation and Adaptive Discretization Methods in Computational Fluid Dynamics, 2002.

[22]Jones, W. L. and Cross, A. E., "Electrostatic Probe Measurements of Plasma Parameters for Two Reentry Flight Experiments at 25,000 Feet per Second," Nasa tn d-6617, Washington, DC, Feb. 1972.

[23]Vincenti, W. and Charles H. Kruger, J., *Introduction to Physical Gas Dynamics*, Krieger, 1965.

[24]Park, C., "On Convergence of Computation of Chemically Reacting Flows," *23rd AIAA Aerospace Science Meeting*, AIAA Paper 1985-0247, Reno, NV, Jan. 1985.

[25]Bussing, T. R. A. and Eberhardt, S., "Chemistry Associated with Hypersonic Vehicles," *Journal of Thermophysics and Heat Transfer*, Vol. 3, No. 3, 1989, pp. 245–253.

A. Chemical Model

A two-species Nitrogen chemical model is used with the following chemical reactions:

$$N_2 + N_2 \longleftrightarrow 2N + N_2, \tag{28a}$$
$$N_2 + N \longleftrightarrow 3N. \tag{28b}$$
$$\tag{28c}$$

The extent of each of the chemical reactions can be determined using classical statistical mechanics[23] and the Law of Mass Action.

$$R_i = -k_{f_i} \prod_{j=reactants_i} \left(\frac{\rho_j}{M_j}\right) + k_{b_i} \prod_{k=products_i} \left(\frac{\rho_k}{M_k}\right), \tag{29}$$

where the chemical rate constants k_f and k_b in Eqn. (29) are Arrhenius-type relations with parameters $C_{f_m}, \eta_m, \theta_m$ and K_{eq} determined experimentally.[24,25]

$$k_{f_m} = k_{f_m}(\bar{T}) = C_{f_m} \bar{T}^{\eta_m} \exp -\theta_m/\bar{T}, \tag{30a}$$
$$k_{b_m} = k_{b_m}(\bar{T}) = k_{f_m}/K_{eq}(\bar{T}), \tag{30b}$$
$$K_{eq_m} = K_{eq_m}((\bar{T}/T_{ref}) = Z) = \exp\left(A_{1_m} + A_{2_m} Z + A_{3_m} Z^2 + A_{4_m} Z^3 + A_{5_m} Z^4\right). \tag{30c}$$

Each of the rate constants enumerated in Eqns. (30a-30c) are temperature dependent. The appropriate temperature, $\bar{T}$ depends on the type of reaction and the collision partners. The chemical system is coupled to the flow equations via source terms, w_s, that are determined by summing the appropriate extent of reaction, Eqn. (29), corresponding to the chemical reactions Eqns. (28a & 28b) where the species appears as either a product or a reactant.

$$w_s = M_s \left(- \sum_{\{i:s\in products_i\}} R_i + \sum_{\{j:s\in reactants_j\}} R_j \right). \tag{31}$$

$$R_1 = -k_{f_{1,m}} \left(\frac{\rho_{N_2}}{M_{N_2}}\right)\left(\frac{\rho_{N_2}}{M_{N_2}}\right) + k_{b_{1,m}} \left(\frac{\rho_N}{M_N}\right)\left(\frac{\rho_N}{M_N}\right)\left(\frac{\rho_{N_2}}{M_{N_2}}\right) \tag{32a}$$
$$R_2 = -k_{f_{1,m}} \left(\frac{\rho_{N_2}}{M_{N_2}}\right)\left(\frac{\rho_N}{M_N}\right) + k_{b_{1,m}} \left(\frac{\rho_N}{M_N}\right)\left(\frac{\rho_N}{M_N}\right)\left(\frac{\rho_N}{M_N}\right) \tag{32b}$$
$$\tag{32c}$$

$$\dot{w}_{N_2} = M_{N_2}\left(R_1 + R_2\right), \tag{33a}$$
$$\dot{w}_N = M_N\left(-2R_2 - 2R_1\right). \tag{33b}$$
$$\tag{33c}$$

B. Fluid Dynamics Model

The source and energy exchange terms appearing on the right hand side of Eqns. (1a-1d) manage the interactions between the constituents of the multi-species flow field due to molecular collisions and external forces. Momentum transfer between species is determined by applying methods from kinetic theory and assuming each species velocity distribution function has a Maxwellian form centered about the mean velocity of the species.

$$f_{s_i}^{coll} = n_s M_s \sum_r (u_{r_i} - u_{s_i}) \frac{n_r}{3 n_s k T_s} \int \sigma_{s,r} (c_{s_k} c_{s_k})^{3/2} f_s dc_s, \tag{34a}$$
$$= \rho_s \sum_r \nu_{s,r}^* (u_{r_i} - u_{s_i}), \tag{34b}$$

where $\nu^*_{s,r}$ is the collision frequency between species s and r and the collision cross section, $\sigma_{s,r}$, depends on the collision partners. Energy exchange between species and between different modes of energy storage is modeled by the terms in Q_s,

$$q_s^{coll} = \sum_r q^{elastic}_{T_r - T_s} - \sum_m q^{inelastic}_{T_s - V_m}. \tag{35}$$

The first term represents energy transferred to s from r through elastic collisions, while the second models the transfer of energy from the translational-rotational modes of s to the vibrational energy of all diatomic species, p, from inelastic particle collisions.

$$q^{elastic}_{T_r - T_s} = -\frac{M_s^2}{M_r} n_r \left(1 - \frac{T_r}{T_s}\right) \int \sigma_{s,r} (c_{s_k} c_{s_k})^{3/2} f_s dc_s, \tag{36a}$$

$$= 2\rho_r \nu^*_{s,r} c_{v_r} \frac{M_r}{M_s} \left(T_r - T_s\right), \tag{36b}$$

Translational-vibrational exchanges are described by a Landau-Teller relation between species r and species s,

$$q^{inelastic}_{T_r - V_s} = \rho_s \frac{E^*_{vib_s}(T) - E_{vib_s}}{\left\langle \tau_{s_{L-T}} \right\rangle}, \tag{37}$$

with vibrational relaxation time,

$$\left\langle \tau_{s_{L-T}} \right\rangle = \frac{\sum_r N_r}{\sum_r N_r / \tau_{r,s_{L-T}}}, \qquad \text{for } r \neq e. \tag{38}$$

Landau-Teller inter-species relaxation time (and constants),

$$\tau_{r,s_{L-T}} = \frac{1}{p} \exp\left[A_{r,s}(T^{-1/3} - 0.015\mu_{r,s}^{1/4}) - 18.42\right], \qquad p \text{ in atm,}. \tag{39}$$

$$A_{r,s} = 1.16 \times 10^{-3} \mu_{r,s}^{1/2} \theta_{v_s}^{4/3}. \tag{40}$$

$$\mu_{r,s} = \frac{M_r M_s}{M_r + M_s}. \tag{41}$$